

Lignin-derived magnetic activated carbons for effective methylene blue removal

*Lu Yu^{1,2}, David J. Keffer², Chien-Te Hsieh^{*3}, Jakob R. Scroggins^{1,2}, Hao Chen⁴, Sheng Dai^{4,5}, David P. Harper^{*,1,2}*

¹ Center for Renewable Carbon, Institute of Agriculture, The University of Tennessee, Knoxville, Tennessee 37996, United States

² Department of Materials Science and Engineering, The University of Tennessee, Knoxville, Knoxville, Tennessee 37996, United States

³ Department of Chemical Engineering and Materials Science, Yuan Ze University, Taoyuan 32003, Taiwan

⁴ Department of Chemistry, The University of Tennessee, Knoxville, TN 37996, United States

⁵ Chemical Sciences Division, Oak Ridge National Laboratory, Oak Ridge, TN 37831, United States

* Corresponding authors' email:

dharper4@utk.edu (Prof. D.P. Harper) and cthsieh@saturn.yzu.edu.tw (Prof. C.T. Hsieh)

ABSTRACT

Large-scale environmental remediation of polluted water requires an effective and recyclable adsorbent produced from an abundant, low-cost, and renewable feedstock via a simple processing procedure. In this work, we demonstrate that lignin-derived magnetic activated carbons (mACs) uniquely satisfy these five criteria for (i) high-performance adsorption, (ii) high regeneration efficiency, (iii) feedstock economic and environmental viability, (iv) single-step processing and (v) large-scale production. The mACs are synthesized via an efficient co-carbonization and activation with simultaneous impregnation of ferric sulfate. The Langmuir model closely fits the adsorption of methylene blue (MB) by mACs within the temperature range of 298–323 K, where the adsorption capacity increases as temperature increases. This capacity increased from 55.0 mg g⁻¹ to 220.2 mg g⁻¹ with the presence of magnetic nanoparticles. In addition, the magnetite nanoparticles on the ACs surface significantly improve its recycling ability with the removal percentage above 95% after four cycles for 5:1 mAC.

KEYWORDS: Lignin, Activated carbon, Magnetite, Adsorption, Dye removal

1. INTRODUCTION

Dyes produced via industrial activities have become one of the most severe water pollutants and cause environmental concerns. With the increasing need for ecologic protection and sustainable development, water purification has been a critical technique to address this pollution problem. Various ways, including membrane separation,¹ photocatalysis,^{2,3} biodegradation⁴, and adsorption⁵, have been applied in this field. Among these, adsorption offers a practical and low-cost approach.⁵⁻⁷ Activated carbon materials (ACs) are widely used as adsorbents for many organic and inorganic environmental pollutants industrially as they possess high surface area, low cost, and high surface reactivity.^{8,9} After use, the carbon adsorbents are hard to collect and recycle. However, magnetic activated carbon composites offer a potential efficient solution. Compared with conventional carbon adsorbents, magnetizing the adsorbents allows for easy separation from the solutions via an external magnetic field to collect and recycle multiple times. Decorating adsorbent surfaces with magnetic nanoparticles significantly improve the adsorption performance by enhancing the electrostatic interaction between metal oxides and organic pollutants.^{10,11}

Magnetic carbon composites have been synthesized from various precursors, such as coconut,¹² graphene oxide,¹³ carbon nanotubes,¹⁴ peanut shell,¹⁵ cotton woven,¹⁶ citrus limetta peels,¹⁷ and so on.¹⁸ In addition to the choice of feedstock, the synthesis method is also a significant factor in the cost and efficiency of producing mAC for large-scale applications. Co-precipitation and hydrothermal synthesis are the most used methods to decorate magnetite onto carbon composites.¹⁹⁻²² However, for most of the previous work, additional steps are involved, which increases the complexity and cost. Wang *et al.*¹³ used a mixture of FeCl₃ and graphene oxide as precursors and heated in an autoclave for 6 hrs, achieving a maximum adsorption capacity of 65.79 mg g⁻¹ for methylene blue (MB). Yu *et al.*¹⁴ performed one-pot oxidation of multi-walled carbon

nanotubes (MWCNTs) and Fe catalyst particles, yielding magnetic MWCNTs with maximum adsorption capacities of 227.05, 138.04, 63.34, 249.44, and 105.59 mg g⁻¹ for ethylbenzene, *m*-xylene, *o*-xylene, *p*-xylene, and toluene, respectively. Liu *et al.* produced Fe₃O₄/AC composites via diol thermal decomposition for rhodamine B (RhB) and methyl orange (MO) adsorption. They doped AC by reacting Fe(acetylacetonate)₃ in benzyl alcohol at N₂ atmosphere to yield Fe₃O₄/AC. The maximum adsorption capacities of 182.48 and 150.35 mg g⁻¹ for RhB and MO, respectively, for the composite.⁸

Lignin is an attractive feedstock for carbon materials because it is low-cost, renewable, and available in abundant quantities. Lignin is produced at a scale of 50-70 million tons annually as a byproduct of pulp and paper production.^{23, 24} Work has demonstrated converting lignin into high-value carbon materials with varying functional linkages controlled by feedstock and processing.²⁵⁻²⁸ García-Mateos *et al.*²⁹ used lignin as a precursor to develop carbon fibers via electrospinning and applied as free-standing electrodes for supercapacitors. Wang *et al.*³⁰ conducted chemical activation with apricot shell lignin as a precursor and investigated the textural properties of the developed activated carbons. Zhou *et al.*³¹ adopted Kraft lignin as a precursor and conducted chemical activation to develop activated carbons for electrochemical energy storage. Wen *et al.*³² adopted Kraft lignin as a carbon source to develop magnetic bio-activated carbons for phosphorus removal and achieved maximum adsorption capacity of 69.80 mg-P/g. Ma *et al.*³³ prepared magnetic lignin-based carbon nanoparticles for methylene orange adsorption with a maximum adsorption capacity of 113.0 mg g⁻¹.

Within the above scope, we employ Kraft lignin (KL) as the carbon source and ferric sulfate as the precursor for mACs applied co-carbonization and activation. This concurrent synthetic route allows the synthesis of magnetic nanoparticles on carbon to occur simultaneously with activation.

The iron serves both as a catalyst for AC formation and a precursor for active magnetic sites. Based on previous work,³⁴ lignin-based ACs primarily contain a complex microporous structure that limits accessibility to ions.^{26, 35, 36} With the impregnation of iron into lignin, surface area and mesopore fraction are greatly improved, thus increasing the porous accessibility toward molecular adsorption in the liquid phase. The adsorption performance of mACs is evaluated by MB dye. The introduction of magnetite nanoparticles on the mACs leads to improved adsorption capacity and benefits the ease of recovery. We demonstrate that lignin-derived mACs are high-performance adsorbents synthesized from an economically and environmentally viable feedstock synthesized via a single-step manufacturing process.

2. EXPERIMENTAL SECTION

2.1. Preparation of mACs adsorbent.

The mAC was produced from commercial Kraft lignin (Indulin AT, Ingevity; Charleston, SC) (KL). The ferric sulfate was purchased from MP Biomedicals (Solon, OH). The mACs were synthesized by impregnating KL with ferric sulfate at different mass ratios (5:1, 10:1, and 20:1 KL:ferric sulfate) in the ceramic boat. The precursor was carbonized at 800°C with nitrogen flow for 1 hour in the tube furnace. Without removal from the furnace, the carbonized magnetic carbons were exposed to steam activation (with the absolute humidity $\sim 19 \text{ g m}^{-3}$) at 800°C for 30 min, as shown in Figure 1. The produced samples were ball-milled (PM100 RETSCH) at 400 revolutions per minute for 30 min to obtain powder mAC samples.

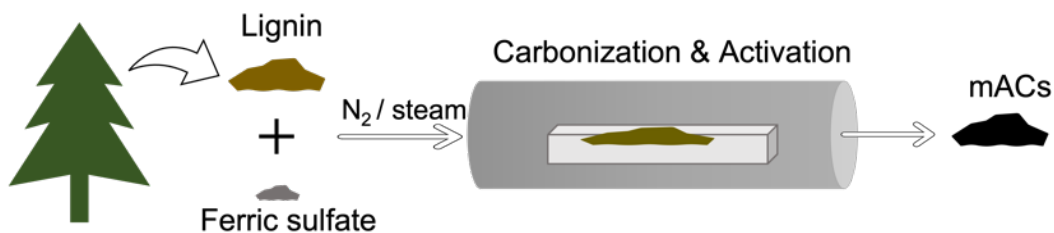


Figure 1. Schematic of mACs preparation via carbonization and activation of kraft lignin and ferric sulfate.

2.2. Materials characterization.

X-ray diffraction (XRD) spectra were collected on an Empyrean diffractometer (Panalytical) with Cu – $K\alpha$ radiation. The morphology and elemental mapping images were obtained by scanning electron microscopy (SEM) (Zeiss, EVO MA15) and energy dispersive x-ray spectroscopy (EDS) (Bruker xFlash 6130) at a magnification of 2,000 respectively. X-ray photoelectron spectroscopy (XPS) was conducted using a Kratos AXIS Ultra DLD XPS system, equipped with a hemispherical energy analyzer and a monochromatic Al $K\alpha$ source, operated at 15 keV and 150 W. The pass energy was fixed at 40 eV for the high-resolution scans and 160 eV for survey scans. Carbon C1s peak at 248.8 eV was used as a reference for charge correction. The porous structures of samples were evaluated via N_2 adsorption isotherms measured by a TriStar 3000 volumetric adsorption analyzer (Micromeritics Instrument Corp.). Specific surface areas (S_{BET}) were calculated based on Brunauer-Emmett-Teller (BET) equation, and pore volumes were derived by the Barrett-Joyner-Halenda (BJH) equation. Sample pore size distribution was determined by density function theory (DFT) calculations. The magnetic properties of the samples were measured with a SQUID vibrating sample magnetometer (Quantum Design, Inc). Zeta potential measurements were measured at various solution pH values with the sample concentration at 1 mg ml^{-1} using a Malvern Zetasizer.

2.3. Liquid-phase adsorption evaluation.

MB (Sigma) solutions were prepared with different concentrations (from 100 – 1200 mg L^{-1}) by mixing in an ultrasonic bath for 24 hrs at room temperature. The concentration of MB solutions was measured by ultraviolet-visible (UV-vis) spectroscopy (Thermo Scientific) at 665

nm. First, a calibration curve was obtained from a series of dye solutions of known dye concentration, as shown below:

$$y = 0.157 * x + 0.001 \quad (1)$$

where x (mg L^{-1}) is concentration, and y is the adsorption intensity. Next, 10 mg mACs and AC were immersed in 5 ml MB solutions of different concentrations (from 100 – 1200 mg L^{-1}) for 48 hrs. The top solution was collected in a 1.5 ml centrifuge tube, and all the samples were centrifugated at 10000 rpm for 5 min before measuring UV-vis. Then the residual concentrations were calculated based on the calibration curve. The effect of solution pH values on the adsorption performance is evaluated by adjusting the pH values from 3 to 9 with the H_2SO_4 and NaOH solutions.

The reusability was tested by placing 0.10 g samples into 50.00 mL MB solution (100 mg L^{-1}) and kept for 24 hrs at room temperature with continuous stirring at 200 rpm. The AC and mAC materials were placed on a stirring plate with and without a magnetic stir bar, respectively. All mACs were effectively mixed on a magnetic stirring plate. The adsorbed samples were washed with 25.00 mL sulfuric acid (0.1 M) and stirred at 200 rpm for 8 hrs. For mACs and AC, the carbons were collected at the bottom of the vials with and without an external magnetic bar after settling. The top solution was removed. The vials were filled with deionized water (DI water) and stirred at 200 rpm for 30 min for washing. The step was repeated until a pH 7 was reached. The neutralized samples were dried in an oven at 105 °C for 30 min. The adsorption-desorption procedure was repeated for four cycles.

3. RESULTS AND DISCUSSION

3.1 Characterization of mACs

The mAC samples produced increased XRD intensities at lower mass ratios of AC to ferric sulfate (Figure 2(a)). The broad peak appearing around 24° is assigned to the (002) diffraction peak of amorphous AC. The interlayer distance (d_{002}) is calculated to be ~ 0.37 nm by the Scherrer equation, larger than that of graphite (0.335 nm). Diffraction peaks characteristic of Fe_3O_4 are present at $2\theta = 30^\circ, 35.3^\circ, 43.5^\circ, 53.1^\circ, 57^\circ,$ and 62.5° , representing the characteristics of (220), (311), (400), (422), (511), and (440) planes, respectively (as shown in Figure 2(b)), and agrees with the inorganic crystal structure database (ICSD) Card No. 35001ICSD. The peak located at around 33.3° corresponds to (104) plane of hematite ($\alpha\text{-Fe}_2\text{O}_3$).¹² Peaks of the mACs sharpen with increasing iron sulfate content, confirming that more ferric sulfate in the precursors produces more crystalline magnetite in the mAC.

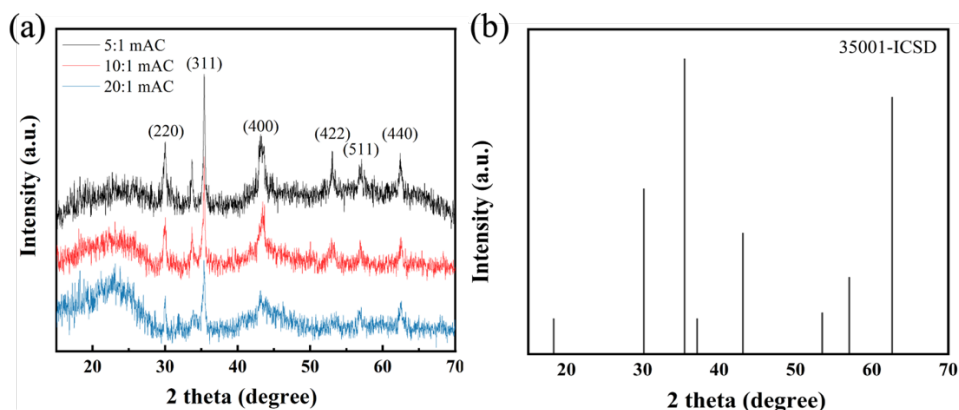


Figure 2. (a) XRD patterns of 5:1 mAC, 10:1 mAC and 20:1 mAC and (b) standard XRD pattern of Fe_3O_4 from 35001 ICSD card.

For further clarification and confirmation, XPS spectroscopy was conducted on the mACs (Figure S1), which proved the presence of iron oxide in the resulting mAC products. Figure S2 The deconvoluted XPS spectra for Fe 2p possess peaks at *ca.* 712.0 eV and 724.0 eV attributed to

Fe 2p_{3/2} and Fe 2p_{1/2}, respectively. Deconvoluted peaks at 710.9 eV and 713.1 eV (Fe 2p_{3/2}) correspond to Fe³⁺ and Fe²⁺ mixed oxide, respectively, and confirm the presence of Fe₃O₄. The other two deconvoluted peaks at 724.1 and 725.9 eV are characteristics of α-Fe₂O₃.¹² Their atomic concentrations of Fe are 2.06%, 1.67%, and 0.64% for 5:1, 10:1, and 20:1 mACs, respectively (see Table S1). The deconvoluted O1s peaks of mAC samples are displayed in Figure S3. The fractions of Fe-O group are 12.5%, 11.5% and 6.5% for 5:1, 10:1 and 20:1 mACs, respectively. Accordingly, the 5:1 mAC shows the highest amount of iron oxide, consistent with the highest loading amount of Fe₂(SO₄)₃ in the precursor. Furthermore, the peaks at 531.5 eV and 532.6-532.7 eV correspond to C=O and C-O bonds, respectively.³⁷ The O1s peaks prove the existence of metal oxides (O⁻), carbonyl, carboxyl, and hydroxyl functional groups.

Iron oxides (magnetite, hematite, and maghemite) are generated during the pyrolysis and activation processes. The reaction of ferric sulfate in a nitrogen environment is described in Eq 2a. The maghemite undergoes structural rearrangement and converts to hematite as the temperature goes up to around 400 °C.^{9, 12} As the temperature increases above 600 °C, some of the hematite reduces to magnetite (Eq 2b). The mACs are synthesized in the CO₂ environment after activation and partial oxidation of magnetite. The complex process leads to a mixture of Fe₃O₄ and Fe₂O₃ on the surface of mACs.



The mACs' XPS C 1s spectra of mACs were decomposed into three peaks centered at 284.8 eV (C=C or C-C), 286.0 eV (C-O), 288.8 eV (C=O) and 289.2-289.4 eV(O-C=O), respectively,³⁸ confirming the presence of oxide functional groups on the surface of porous carbon structures

(Figure 3). The C=O accounts for 9.6%, 8.0% and 7.0%, O-C=O accounts for 9.2%, 12.8% and 11.0%, while C-O accounts for 20.3%, 23.0% and 21.0% of the total integration area for the 5:1, 10:1 and 20:1 mACs, respectively. In order to confirm the presence of MB after adsorption, FTIR spectra of 5:1 mAC before and after MB adsorption and MB were collected and shown in Figure S4. In the MB sample, the strong peak located around 1600 cm^{-1} corresponds to aromatic group of MB, and the peaks located in the range of $1340\text{-}1440\text{ cm}^{-1}$ are attributed to the heterocyclic vibrations of MB skeleton.³⁹ It can be obviously noticed that the intensities of these peaks are increased for the of the 5:1 mAC after MB adsorption, indicating the MB has been adsorbed and covered on the surface of 5:1 mAC.

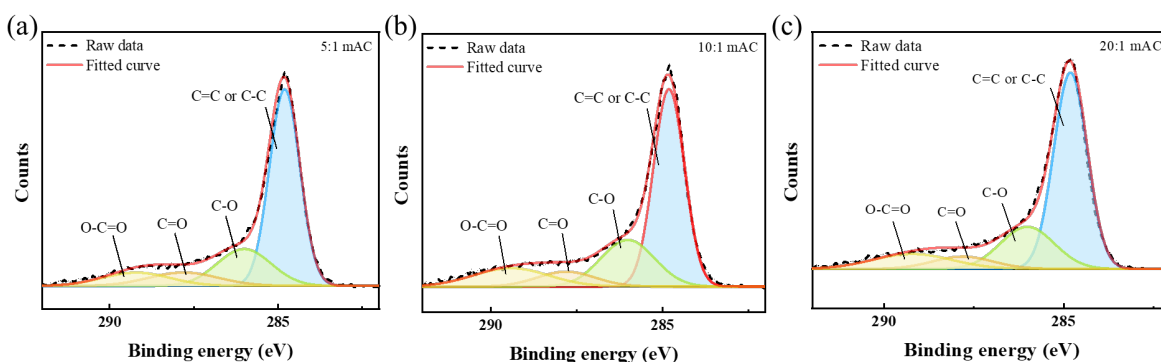


Figure 3. Deconvoluted XPS spectra of C 1s peak for (a) 5:1, (b) 10:1 and (c) 20:1 mACs.

The magnetic properties of mACs and AC were evaluated by the magnetic hysteresis curves. As shown in Figure 4, the magnetic saturation (M_s) values of AC, 20:1 mAC, 10:1 mAC and 5:1 mAC samples are about 0.0, 2.0, 5.6, and 6.6 emu g^{-1} , respectively. This result confirmed the presence of magnetic nanoparticles on the mAC samples and the magnetic saturation values are positively correlated with the impregnation amount of ferric sulfate in the precursor.

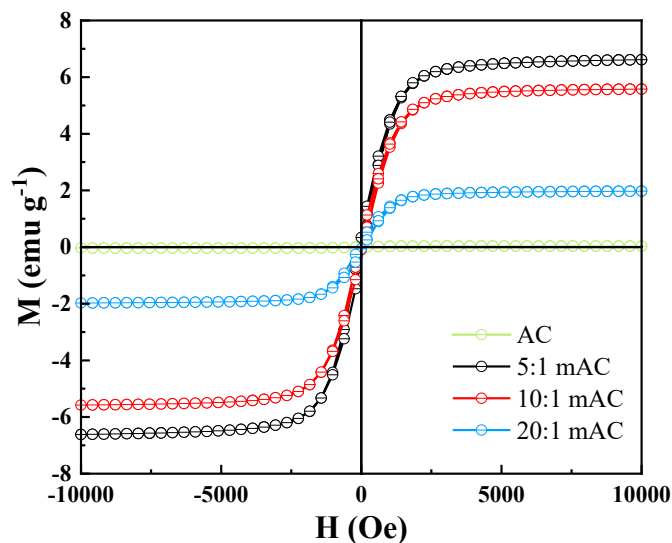


Figure 4. Magnetic hysteresis curves of AC and mAC samples.

The morphological features of the mAC samples were characterized via SEM and EDS maps of Fe. As shown in Figure 5, the average particle size of AC on the 10:1 mAC sample is in the range of 10~20 μm , which is slightly larger than that of the 5:1 mAC (10~15 μm) and 20:1 mAC (5~10 μm). The generated EDS maps of elemental Fe confirm the homogeneous distribution of the iron oxide nanoparticles on the surface of mACs.

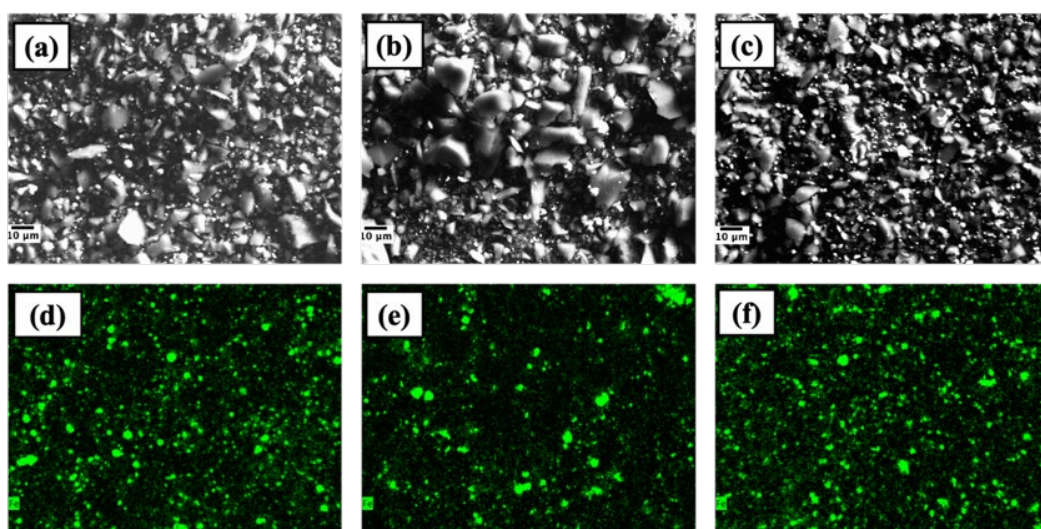


Figure 5. SEM images and EDS maps of Fe element of (a, d) 5:1, (b, e) 10:1 and (c, f) 20:1 mACs.

The pore size distributions of the samples are depicted in Figure 6. The mAC samples possess sharp peaks at pore size ~ 1 nm and broad peaks distributed $\sim 2 - 6$ nm, whereas the pure AC only exhibits a sharp peak at pore size ~ 1.8 nm, demonstrating the microporosity of pure ACs. From the large, broad peak in the range of $2 - 10$ nm, we observe the mesopore fraction decreased in the sequence of $5:1 \text{ mAC} > 20:1 \text{ mAC} > 10:1 \text{ mAC} > \text{AC}$. Table 1 summarizes S_{BET} , micro/mesopores ratio, PV_{micro} , and PV_{meso} . The 5:1, 10:1, and 20:1 mACs have BET surface areas of 528.1, 515.8, and 512.8 $\text{m}^2 \text{g}^{-1}$, with a mesopore ratio of 17.0, 10.3, and 14.7%, respectively. In comparison, AC has a BET surface area of just 318.8 $\text{m}^2 \text{g}^{-1}$ and a mesopore ratio of only 1.6%. The surface area and mesopore volume are significantly increased with the impregnation of $\text{Fe}_2(\text{SO}_4)_3$ in the precursors, demonstrating the role of iron as a catalyst in the process of pyrolysis and activation.^{9, 12} In addition, the iron is oxidized into iron oxide and grown on the surface of ACs during the pyrolysis and activation process, leading to the more porous structures of mACs.⁸

Table 1. Characterization parameters (Fe %, S_{BET} , micropore/mesopore ratio, PV_{micro} , and PV_{meso}) of mACs and AC determined from BET measurement.

Samples	Iron content (atomic conc %)	S_{BET} ($\text{m}^2 \text{g}^{-1}$)	micropore ratio (%)	mesopore ratio (%)	PV_{micro} ($\text{cm}^3 \text{g}^{-1}$)	PV_{meso} ($\text{cm}^3 \text{g}^{-1}$)
5 : 1 mAC	2.06	528.1	83.0	17.0	0.21	0.09
10 : 1 mAC	1.67	515.8	89.7	10.3	0.22	0.05
20 : 1 mAC	0.64	512.8	85.3	14.7	0.21	0.08
AC	0	318.8	98.4	1.6	0.15	0.01

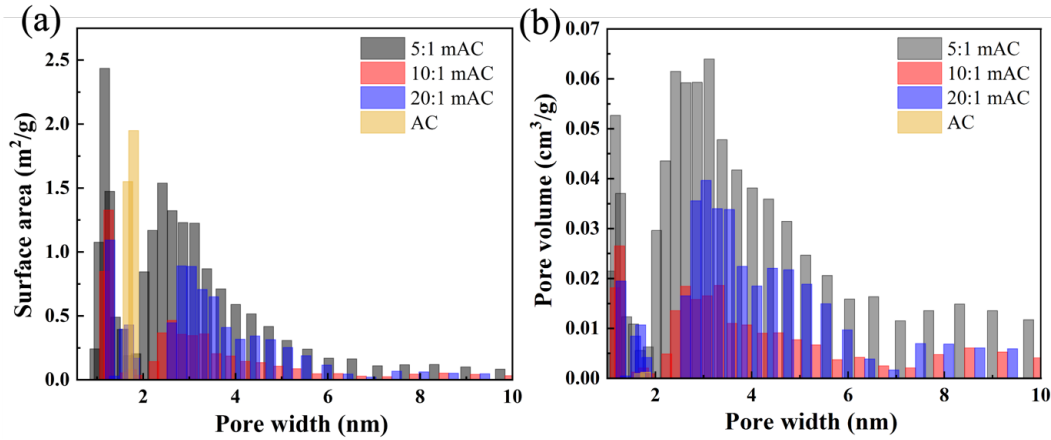


Figure 6. (a, b) DFT pore size distributions of mACs and AC.

3.2 Adsorption performance of mACs

3.2.1 Adsorption isotherm

MB adsorption isotherms on the carbon samples were fit to the Langmuir model:

$$q_e = \frac{q_m K_L C_e}{1 + K_L C_e} \quad (3)$$

Where q_e (mg g⁻¹) is the amount of MB adsorbed per unit mass of carbon, C_e (mg L⁻¹) is the concentration of MB when the solution reaches the maximum adsorption amount of the carbon, q_m (mg g⁻¹), K_L (L mg⁻¹) is the Langmuir equilibrium constant. As shown in Figure 7(a), the Langmuir model fits the experimental data ($R^2 > 0.999$), indicating the assumption of monolayer adsorption is valid. The maximum adsorption capacities of mACs and AC are presented in Table 2. The theoretical maximum adsorption is greatly increased from 55.0 mg g⁻¹ of AC to 220.2 mg g⁻¹ for the 5:1 mAC. We assume that the higher surface area and pore volume allows for more accessible adsorption sites available for MB. Introducing iron in the precursors leads to higher surface area and greater mesopore ratio for the mACs over AC, thus MB adsorption. In addition, the maximum adsorption capacities for 5:1, 10:1, 20:1 mAC are 220.2, 151.1, 99.8 and 55.0 mg g⁻¹, respectively. Given that there is little difference in surface area and benefit from the pore

structure (Table 1), iron oxide's presence on the surface greatly improves the adsorption performance of activated carbons.

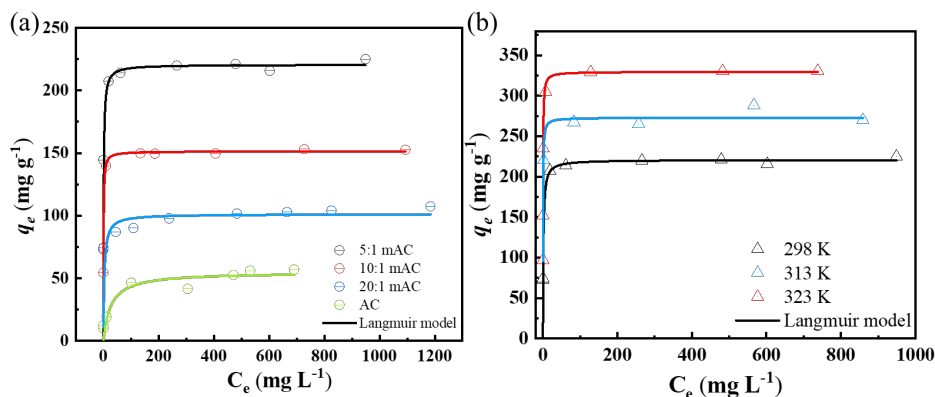


Figure 7. (a) Adsorption isotherm curves fitted by Langmuir model of mACs and AC, (b) Adsorption isotherm curves fitted by Langmuir model of 5:1 mAC under 298, 313, and 323K.

Table 2. Parameters derived from the fits of the Langmuir model to the experimental data for mACs and AC.

Samples	q_m (mg g ⁻¹)	K_L (L mg ⁻¹)	R^2
5:1 mAC	220.2	0.80	0.9999
10:1 mAC	151.1	1.28	0.9999
20:1 mAC	99.8	0.28	0.9998
AC	55.0	0.04	0.9996

3.2.2 Adsorption kinetics

The adsorption rate performance is the critical process metric for commercial applications.⁴⁰ Adsorption rates were measured by immersing 0.10 g samples into 50.00 mL MB solution (500 mg L⁻¹) at room temperature. We observed that the MB adsorption in 5:1 mAC occurs much more quickly than in the pristine AC (Figure S5(a)). The AC takes roughly 8 hrs to reach adsorption of 55 mg g⁻¹, whereas the same loading is obtained within 0.08 hr in the 5:1 mAC. Two mathematical

models, which are pseudo-first order (Eq 4a) and pseudo-second order (Eq 4b) models, were adopted to describe the adsorption kinetics of MB.

$$\ln(q_e - q_t) = \ln(q_e) - k_1 t \quad (4a)$$

$$\frac{t}{q_t} = \frac{1}{k_2 q_e^2} + \frac{t}{q_e} \quad (4b)$$

Where q_e (mg g⁻¹) is the equilibrium adsorption amount of the adsorbent, q_t (mg g⁻¹) is the adsorption amount at t time, k_1 is the pseudo first order rate constant (h⁻¹), k_2 is the pseudo second order rate constant (g/(mg·h)), and t is the contact time (h). To identify the sorption mechanism, both models were fit to the data (Table S2). The pseudo-first order model assumes the adsorption process is dominated by diffusion, whereas the pseudo-second order model describes chemical adsorption.⁴⁰⁻⁴² Both models fit the experimental data. The adsorption process can be further divided into membrane diffusion, intra-particle diffusion, and the actual adsorption steps.^{40, 43} To confirm that the process is not strictly intra-particle diffusion controlled, the intra-particle diffusion model was fit to the experimental data (Figure S5(b)). If the plot of q_t versus $t^{1/2}$ exhibits only one linear section, the adsorption is controlled only by intra-particle diffusion. Conversely, multiple linear sections in the plots represent more than one process.⁴³ As shown in Figure S5(b), the plots consist of two straight lines, confirming that multiple mechanisms control the adsorption layer process. Further, the large intercepts indicate an additional mechanism controlling rate besides intra-particle diffusion.

3.2.3 Temperature effect on the adsorption

The adsorption properties were evaluated at different temperatures (from 298 to 323 K). Figure 6(b) shows the adsorption amount versus equilibrium concentration for the 5:1 mAC sample fitted by the Langmuir model at different temperatures (Table 3). The maximum adsorption capacities reach 329.6, 272.9, and 220.2 mg g⁻¹ at 323, 313, and 298 K, respectively. The

adsorption capacity of 5:1 mAC increases with increasing temperature and indicates an endothermic process promoting the adsorption of MB through a physical process.

Table 3. Adsorption isotherm parameters for MB onto 5:1 mAC at 298, 313, and 323 K.

5:1 mAC	q_m (mg g ⁻¹)	K_L (L mg ⁻¹)	R^2
298K	220.2	0.80	0.9999
313K	272.9	2.60	0.9868
323K	329.6	2.70	0.9699

3.2.4 pH effect on the adsorption

Initial pH of the solution affects the surface charges of the adsorbent, thus influencing the adsorption efficiency. The zeta potentials of mAC 5:1 adsorbent were measured in the pH range of 3 – 9. As shown in Figure 8, as the solution condition changes from acidic to alkaline, the zeta potential of the sample goes from positive (+2.36 mV) to negative (~ -35.67 to -45.60 mV). At extreme acid condition (pH = 3), the abundance of hydrogen ions may compete with cationic MB molecules and occupy some binding sites on the 5:1 mAC,⁴⁴ thus leading to the low MB adsorption capacity. As the pH value increases, the surface functional groups of 5:1 mAC are deprotonated and the adsorption capacity toward cationic MB increases. In alkaline condition (pH = 9), the adsorption capacity decreases a little bit as some Na⁺ are introduced into the solution and might also be adsorbed on the surface of 5:1 mAC.²²

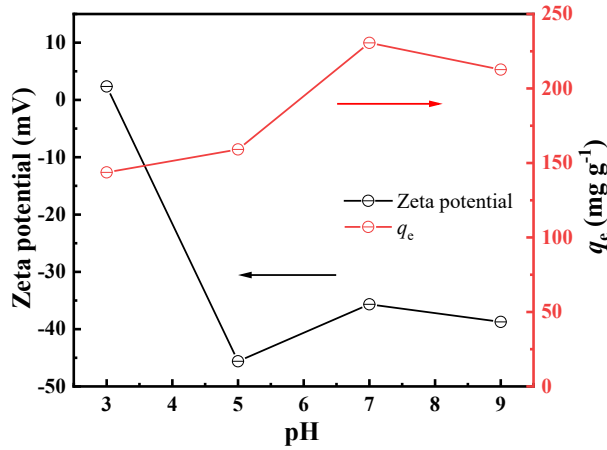


Figure 8. Effect of pH values on the zeta potentials and MB adsorption performance of 5:1 mAC sample.

3.2.5 Adsorption thermodynamics

The adsorption thermodynamics were investigated based on the following equations:

$$K_d = \frac{q_e}{C_e} \quad (5a)$$

$$\Delta G^0 = -RT \ln K^0 \quad (5b)$$

$$\ln K^0 = -\frac{\Delta H^0}{RT} + \frac{\Delta S^0}{R} \quad (5c)$$

where ΔG^0 , ΔH^0 , and ΔS^0 are changes of Gibbs free energy, enthalpy and entropy, respectively.

R is the universal gas constant, which is $8.314 \text{ J mol}^{-1} \text{ K}^{-1}$. T is temperature (K) and K_d is distribution coefficient, which is calculated based on the Eq 5a, and K^0 is calculated when extrapolating C_e to zero.^{9, 13, 45, 46} The value of ΔG^0 is obtained from the Eq 5b, and ΔH^0 and ΔS^0 are determined from the slope and intercept of the linear fit of the plot of $\ln K_d$ versus $1/T$ (Eq 5c).^{13, 47} The obtained values of the thermodynamic parameters are shown in Table 4. The ΔG^0 are negative and decrease with increasing temperature, indicating the MB adsorption process is spontaneous and the spontaneity increases with increasing temperature. The ΔH^0 and ΔS^0 are

18.98 K J mol⁻¹ and 101.35 J K⁻¹ mol⁻¹, respectively, the positive values prove the endothermic and random nature of the adsorption process.

Table 4. Adsorption thermodynamic parameters for MB onto 5:1 mAC at 298, 313, and 323 K.

Temperature (K)	ΔG^0 (KJ mol ⁻¹)	ΔH^0 (KJ mol ⁻¹)	ΔS^0 (J K ⁻¹ mol ⁻¹)
298	-11.31		
313	-12.51	18.98	101.35
323	-13.91		

3.3 Regeneration and recyclability of mACs

Absorbent stability and reusability are crucial for cost effective industrial removal of toxins from water. Owing to the magnetic properties, mACs can be easily collected by an external magnet (Figure 9(b)), which is convenient for recovery and reuse. To assess the regeneration efficiency of the mACs, an external magnet separated MB absorbed carbons. After separation, they were first washed with a sulfuric acid solution. Afterward, the carbons were washed with DI water until neutralized. The adsorption and desorption cycles were repeated for four cycles, and the reusability of samples was determined by removal percentage (%):

$$\text{Removal percentage (\%)} = \frac{C_0 - C_t}{C_0} * 100 \quad (6)$$

where the C_0 (mg L⁻¹) is the initial concentration and C_t (mg L⁻¹) is the concentration at time t.

As shown in Figure 9(a), the 5:1 mAC sample shows excellent adsorption efficiency with the removal percentage above 95% for four cycles. For the 10:1 mAC, the removal percentage is slightly reduced on the 4th cycle but remains at 89.4%, possibly due to the incomplete dye desorption. The 20:1 mAC exhibits a decrease in adsorption efficiency (down to 91.7%) on the 2nd round, and the removal percentages are 86.4%, 63.0% for the 3rd and 4th cycles, respectively. The reusability performance of mACs shows a trend as follows: 5:1 mAC > 10:1 mAC > 20:1 mAC >

AC, demonstrating that the 5:1 mAC possesses the best reusability and remains as an efficient adsorbent even after four cycles. For comparison, the removal percentage of AC drops down from 43.8% for the 1st cycle to 18.8% for the 2nd cycle and loses efficiency (2.4%) at 3rd round recycle. This result supports the observation that the presence of magnetite nanoparticles facilitates the adsorption/desorption process of MB on the samples, and the magnetic nanoparticle loading positively correlates with the reusability of adsorbents.

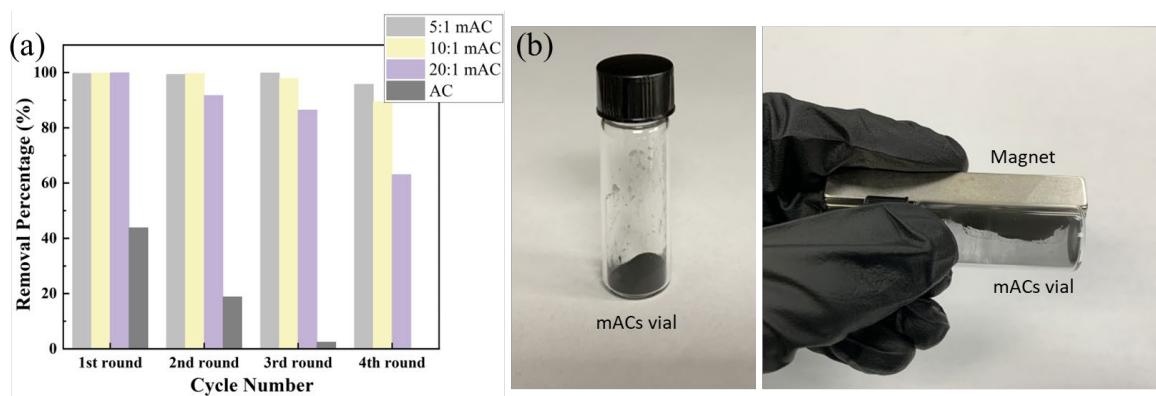


Figure 9. (a) Reusability test of mACs for MB adsorption and (b) images of mACs without and with the external magnet.

The exceptional characteristic of the 5:1 mAC is best expressed as a totality of its adsorption capacity, recyclability, production scale, low-cost processing, and environmental viability. To best communicate this unique combination of traits, we present a comparison radar plot with other published adsorbents, shown in Figure 10. In this discussion, we address the five traits individually. First, we observe that the adsorption capacity of 5:1 mAC toward MB is superior to the other adsorbents in the plot. Second, as for the performance over multiple cycles, magnetic carbon composites demonstrate improved regeneration efficiency. The 5:1 mAC and MACS-700 both maintain adsorption capacitance over 85% after 4 cycles. Third, only the Merck commercial ACs have demonstrated production scale. However, while the 5:1 mAC was produced at gram scale, it has potential for industrial-scale production because the single-step process by which it was

synthesized is similar to processes used in industry. In contrast, most of the magnetic carbon adsorbents, such as the MACS-700, magnetic GO-CNT composite, $\text{Fe}_3\text{O}_4@\text{C}$ NPs, and $\text{GO-Fe}_3\text{O}_4$, were produced via the hydrothermal method, which can only be developed at very small scale. Fourth, as for the safe, facile and low-cost processing, the 5:1 mAC is directly produced via a single step method. There is no corrosive effect on the production facilities and no extra wash step needed. $\text{Fe}_3\text{O}_4@\text{C}$ NPs and MACS-700 samples were developed after three steps. Magnetic GO-CNT composite used more than four steps. G-CNT were synthesized with more than five steps and $\text{GO-Fe}_3\text{O}_4$ even needed more than eight steps. The complicated multi-step processes limit the possibility for industrial applications. Fifth, considering the feedstock economic & environmental viability, renewable and cheap resources are significant factors. Most commercial scaled ACs are produced from coconut shell, while 5:1 mACs are derived from waste stream lignin. The price of commercial lignin is in range of \$100-300 per ton,⁴⁸ while coconut shell price is about \$150/ton.⁴⁹ In comparison, MACS-700 and $\text{Fe}_3\text{O}_4@\text{C}$ NPs used glucose as precursor, while the G-CNT and magnetic GO-CNT composite both used graphite and MWCNT as precursors and $\text{GO-Fe}_3\text{O}_4$ used graphite as precursor. However, in addition to the precursors, there are still extra chemicals, such as acid or alkali solutions, and abundant deionized water involved in the hydrothermal and washing process that lead to the increased cost. From these five perspectives, the 5:1 mAC uniquely provides the optimal combination of technical performance, economic value and sustainability.

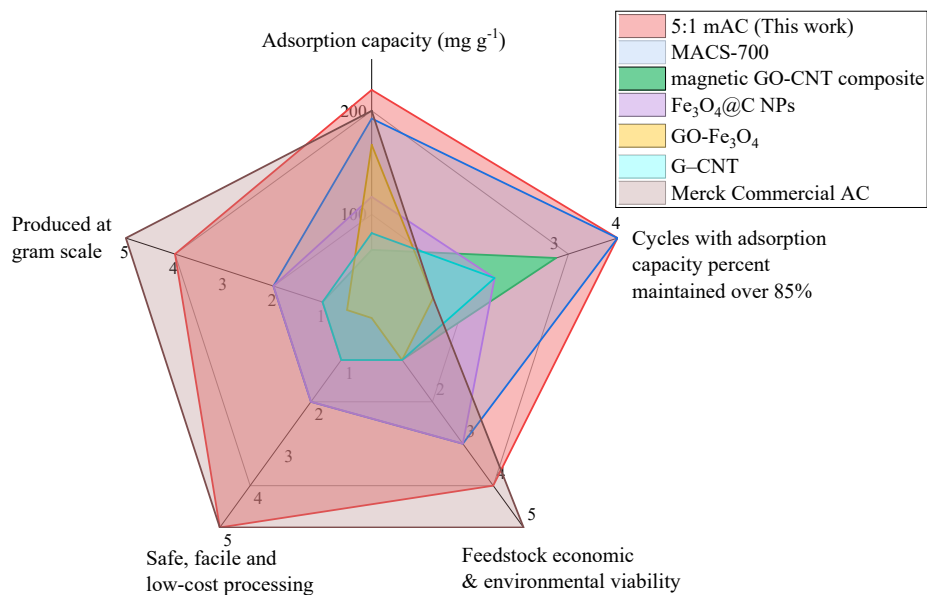


Figure 10. Comparison radar plot (detailed data is shown in Table S3) of adsorption performance toward MB, process and cost of other adsorbents reported.^{13, 22, 50-53}

3.4. Adsorption mechanisms

The atomic scale process behind the adsorption mechanism can arise from multiple factors, including the surface characteristics and heterogeneity, porosity and functional groups of adsorbents, and the molecular structure of adsorbates. For carbon materials, the adsorption between adsorbents and adsorbates occurs primarily through hydrogen bonding, π - π interactions, and electrostatic interactions. As shown in Figure 11, we proposed an adsorption mechanism for MB on mACs. The proposed mechanisms involved are illustrated. The surface functional groups were determined by XPS spectra, and the disordered graphite structure was confirmed by XRD measurement as well as previous work.^{34, 54} The principal interaction should be the π - π interaction between the π -electron system on ACs and aromatic structure of MB, and the hydrogen bonding interactions between the carboxyl/hydroxyl functional groups and MB molecules.^{44, 55, 56} In addition, the electrostatic interactions with cationic MB were introduced as the mAC's surface is

negatively charged (O^-).^{8, 9, 12} Additionally, the introduction of iron oxides on the surface of mAC leads to the vastly improved MB adsorption as well, which should be attributed to the enhanced electrostatic interaction between iron oxides and MB molecules.^{10, 11}

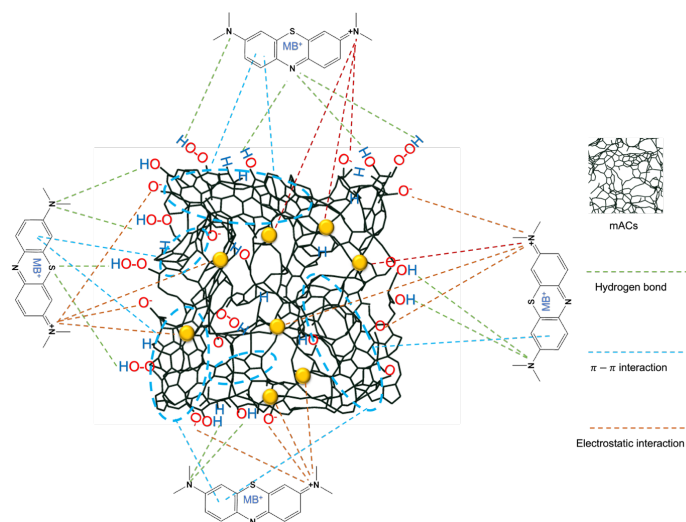


Figure 11. Adsorption mechanisms for MB onto mACs where the yellow dots represent a mixture of iron oxides.

4. CONCLUSIONS

We developed a simple route to synthesize mACs in a one-step process. A mixture of lignin and ferric sulfate were applied as precursors for co-carbonization and activation. Incorporating ferric sulfate into the lignin matrix improved the surface area of mACs with magnetic iron oxides nanoparticles uniformly distributed on the surface. The adsorption of MB occurs primarily through a physical adsorption process on the surface functional groups, π -electron system of the aromatic carbon, and the iron oxides on the surface. These magnetite nanoparticles on ACs enhanced the adsorption capacity via enhanced electrostatic interactions and significantly improved the regeneration efficiency. The maximum adsorption capacity for MB was greatly increased from 55.0 mg g⁻¹ on non-magnetic AC to 220.2 mg g⁻¹ for the 5:1 mAC. The reusability test demonstrated that mACs could be easily separated magnetically and exhibited excellent reusability

with high removal efficiency (> 95%) even after four use cycles. A comparison of the 5:1 mAC with other AC adsorbents in the literature demonstrates that it possesses a unique set of characteristics that make it a superior material for industrial-scale water remediation. In conclusion, this work demonstrates that lignin-derived magnetic activated carbons are high performance adsorbents, synthesized from a lignin feedstock that is both economically and environmentally viable via a simple, single-step process.

ACKNOWLEDGMENTS

The authors would like to thank Dr. Stavros G Karakalos (University of South Carolina) for his help for conducting XPS characterization. The authors would also like to thank Alicia Zahnen for her help conducting experiments. L. Y. received partial support from the Center for Materials Processing, a Tennessee Higher Education Commission (THEC). This research was supported by a grant from the U.S. Department of Energy BioEnergy Technologies Office through the Biomass Research and Development Initiative award DE-EE0008353.0000. D.P.H. acknowledges support from the USDA National Institute of Food and Agriculture Hatch Project 1012359. H. C. and S. D. (characterization) were supported by Division of Chemical Sciences, Geosciences, and Biosciences, Office of Basic Energy Sciences, U.S. Department of Energy.

Supporting Information:

Table S1. Composition and elemental analysis of mACs obtained from deconvolution and integration of XPS peaks.

Table S2. Kinetic parameters of pseudo-first order, pseudo-second order model fits.

Table S3. Parameters of comparison radar plot of adsorption performance toward MB, process and cost of other adsorbents reported.^{13, 22, 50-53}

Figure S1. XPS survey spectra for (a) mAC_5_1, (b) mAC_10_1 and (c) mAC_20_1.

Figure S2. Deconvoluted XPS spectra of Fe 2p peak for (a) 5:1 mAC, (b) 10:1 mAC and (c) 20:1 mAC.

Figure S3. Deconvoluted XPS spectra of O 1s peak for (a) 5:1 mAC, (b) 10:1 mAC and (c) 20:1 mAC.

Figure S4. FTIR spectra of 5:1 mAC (before and after MB adsorption) and MB.

Figure S5. (a) Adsorbed amounts of MB as a function of time for 5:1 mAC and AC, (b) Kinetics of MB adsorption according to the intra-particle diffusion model.

REFERENCES

1. van Voorthuizen, E.; Zwijnenburg, A.; van der Meer, W.; Temmink, H., Biological black water treatment combined with membrane separation. *Water Res* **2008**, *42* (16), 4334-40.
2. Fazal, T.; Razzaq, A.; Javed, F.; Hafeez, A.; Rashid, N.; Amjad, U. S.; Ur Rehman, M. S.; Faisal, A.; Rehman, F., Integrating adsorption and photocatalysis: A cost effective strategy for textile wastewater treatment using hybrid biochar-TiO₂ composite. *J Hazard Mater* **2020**, *390*, 121623.
3. Talukdar, K.; Jun, B. M.; Yoon, Y.; Kim, Y.; Fayyaz, A.; Park, C. M., Novel Z-scheme Ag₃PO₄/Fe₃O₄-activated biochar photocatalyst with enhanced visible-light catalytic performance toward degradation of bisphenol A. *J Hazard Mater* **2020**, *398*, 123025.
4. Ghoreishi, S. M.; Haghighi, R., Chemical catalytic reaction and biological oxidation for treatment of non-biodegradable textile effluent. *Chemical Engineering Journal* **2003**, *95* (1-3), 163-169.
5. Liang, L.; Zhang, S.; Goenaga, G. A.; Meng, X.; Zawodzinski, T. A.; Ragauskas, A. J., Chemically Cross-Linked Cellulose Nanocrystal Aerogels for Effective Removal of Cation Dye. *Front Chem* **2020**, *8*, 570.
6. Chang, J.; Ma, J.; Ma, Q.; Zhang, D.; Qiao, N.; Hu, M.; Ma, H., Adsorption of methylene blue onto Fe₃O₄/activated montmorillonite nanocomposite. *Applied Clay Science* **2016**, *119*, 132-140.
7. Chen, J.; Yuan, M.; Cai, W.; Wei, J.; Zhou, J.; Liu, P.; Yang, Z.; Luo, J.; Xia, Q.; Cai, Z., Constructing the frustrated Lewis pairs within N,S-codoped carbon to reveal the role of adjacent heteroatom sites for highly effective removal of heavy metal ions. *Chemical Engineering Journal* **2021**, *422*, 130153.
8. Liu, X.; Tian, J.; Li, Y.; Sun, N.; Mi, S.; Xie, Y.; Chen, Z., Enhanced dyes adsorption from wastewater via Fe₃O₄ nanoparticles functionalized activated carbon. *J Hazard Mater* **2019**, *373*, 397-407.
9. Feiqiang, G.; Xiaolei, L.; Xiaochen, J.; Xingmin, Z.; Chenglong, G.; Zhonghao, R., Characteristics and toxic dye adsorption of magnetic activated carbon prepared from biomass waste by modified one-step synthesis. *Colloids and Surfaces A: Physicochemical and Engineering Aspects* **2018**, *555*, 43-54.
10. Han, T.; Lu, X.; Sun, Y.; Jiang, J.; Yang, W.; Jonsson, P. G., Magnetic bio-activated carbon production from lignin via a streamlined process and its use in phosphate removal from aqueous solutions. *Sci Total Environ* **2020**, *708*, 135069.
11. Vikrant, K.; Kim, K. H.; Ok, Y. S.; Tsang, D. C. W.; Tsang, Y. F.; Giri, B. S.; Singh, R. S., Engineered/designer biochar for the removal of phosphate in water and wastewater. *Sci Total Environ* **2018**, *616-617*, 1242-1260.
12. Cazetta, A. L.; Pezoti, O.; Bedin, K. C.; Silva, T. L.; Paesano Junior, A.; Asefa, T.; Almeida, V. C., Magnetic Activated Carbon Derived from Biomass Waste by Concurrent Synthesis: Efficient Adsorbent for Toxic Dyes. *ACS Sustainable Chemistry & Engineering* **2016**, *4* (3), 1058-1068.
13. Wang, P.; Cao, M.; Wang, C.; Ao, Y.; Hou, J.; Qian, J., Kinetics and thermodynamics of adsorption of methylene blue by a magnetic graphene-carbon nanotube composite. *Applied Surface Science* **2014**, *290*, 116-124.

14. Yu, F.; Ma, J.; Wang, J.; Zhang, M.; Zheng, J., Magnetic iron oxide nanoparticles functionalized multi-walled carbon nanotubes for toluene, ethylbenzene and xylene removal from aqueous solution. *Chemosphere* **2016**, *146*, 162-72.
15. Cai, W.; Li, Z.; Wei, J.; Liu, Y., Synthesis of peanut shell based magnetic activated carbon with excellent adsorption performance towards electroplating wastewater. *Chemical Engineering Research and Design* **2018**, *140*, 23-32.
16. Xu, Z.; Zhou, Y.; Sun, Z.; Zhang, D.; Huang, Y.; Gu, S.; Chen, W., Understanding reactions and pore-forming mechanisms between waste cotton woven and FeCl₃ during the synthesis of magnetic activated carbon. *Chemosphere* **2020**, *241*, 125120.
17. Siddique, A.; Nayak, A. K.; Singh, J., Synthesis of FeCl₃-activated carbon derived from waste Citrus limetta peels for removal of fluoride: An eco-friendly approach for the treatment of groundwater and bio-waste collectively. *Groundwater for Sustainable Development* **2020**, *10*, 100339.
18. Dai, J.; Tian, S.; Jiang, Y.; Chang, Z.; Xie, A.; Zhang, R.; Li, C.; Yan, Y., Fe₃C/Fe/C Magnetic Hierarchical Porous Carbon with Micromesopores for Highly Efficient Chloramphenicol Adsorption: Magnetization, Graphitization, and Adsorption Properties Investigation. *Industrial & Engineering Chemistry Research* **2018**, *57* (10), 3510-3522.
19. Nethaji, S.; Sivasamy, A.; Mandal, A. B., Preparation and characterization of corn cob activated carbon coated with nano-sized magnetite particles for the removal of Cr(VI). *Bioresour Technol* **2013**, *134*, 94-100.
20. Yang, Z.-F.; Li, L.-Y.; Hsieh, C.-T.; Juang, R.-S., Co-precipitation of magnetic Fe₃O₄ nanoparticles onto carbon nanotubes for removal of copper ions from aqueous solution. *Journal of the Taiwan Institute of Chemical Engineers* **2018**, *82*, 56-63.
21. Zhu, X.; Liu, Y.; Qian, F.; Zhou, C.; Zhang, S.; Chen, J., Preparation of magnetic porous carbon from waste hydrochar by simultaneous activation and magnetization for tetracycline removal. *Bioresour Technol* **2014**, *154*, 209-14.
22. Wu, R.; Liu, J.-H.; Zhao, L.; Zhang, X.; Xie, J.; Yu, B.; Ma, X.; Yang, S.-T.; Wang, H.; Liu, Y., Hydrothermal preparation of magnetic Fe₃O₄@C nanoparticles for dye adsorption. *Journal of Environmental Chemical Engineering* **2014**, *2* (2), 907-913.
23. Suhas; Carrott, P. J.; Ribeiro Carrott, M. M., Lignin--from Natural Adsorbent to Activated Carbon: A Review. *Bioresour Technol* **2007**, *98* (12), 2301-12.
24. Bajwa, D. S.; Pourhashem, G.; Ullah, A. H.; Bajwa, S. G., A concise review of current lignin production, applications, products and their environmental impact. *Industrial Crops and Products* **2019**, *139*.
25. García-Negrón, V.; Phillip, N. D.; Li, J.; Daniel, C.; Wood, D.; Keffer, D. J.; Rios, O.; Harper, D. P., Processing–Structure–Property Relationships for Lignin -Based Carbonaceous Materials Used in Energy-Storage Applications. *Energy Technology* **2017**, *5* (8), 1311-1321.
26. Maldhure, A. V.; Ekhe, J. D., Preparation and characterizations of microwave assisted activated carbons from industrial waste lignin for Cu(II) sorption. *Chemical Engineering Journal* **2011**, *168* (3), 1103-1111.
27. Arkhilin, M. A.; Bogdanovich, N. I.; Efremova, S. V., Synthesis of Magneto-Susceptible Adsorbents on the Basis of Hydrolytic Lignin Using Iron (III) Oxide. *Lesnoy Zhurnal (Russian Forestry Journal)* **2018**, (4), 150-160 0536-1036.
28. Dai, L.; Li, Y.; Liu, R.; Si, C.; Ni, Y., Green mussel-inspired lignin magnetic nanoparticles with high adsorptive capacity and environmental friendliness for chromium(III) removal. *International Journal of Biological Macromolecules* **2019**, *132*, 478-486.

29. García-Mateos, F. J.; Ruiz-Rosas, R.; María Rosas, J.; Morallón, E.; Cazorla-Amorós, D.; Rodríguez-Mirasol, J.; Cordero, T., Activation of electrospun lignin-based carbon fibers and their performance as self-standing supercapacitor electrodes. *Separation and Purification Technology* **2020**, *241*, 116724.
30. Wang, L.; Feng, X.; Li, X.; Ma, H.; Wu, J.; Chen, Y.; Zhou, J., Valorization of lignin: Application of lignin-derived activated carbon in capacitors and investigation of its textural properties and electrochemical performance. *Diamond and Related Materials* **2022**, *122*, 108791.
31. Zhou, B.; Liu, W.; Gong, Y.; Dong, L.; Deng, Y., High-performance pseudocapacitors from kraft lignin modified active carbon. *Electrochimica Acta* **2019**, *320*, 134640.
32. Wen, Y.; Zheng, Z.; Wang, S.; Han, T.; Yang, W.; Jönsson, P. G., Magnetic bio-activated carbons production using different process parameters for phosphorus removal from artificially prepared phosphorus-rich and domestic wastewater. *Chemosphere* **2021**, *271*, 129561.
33. Ma, Y.-z.; Zheng, D.-f.; Mo, Z.-y.; Dong, R.-j.; Qiu, X.-q., Magnetic lignin-based carbon nanoparticles and the adsorption for removal of methyl orange. *Colloids and Surfaces A: Physicochemical and Engineering Aspects* **2018**, *559*, 226-234.
34. Yu, L.; Hsieh, C. T.; Keffer, D. J.; Chen, H.; Goenaga, G. A.; Dai, S.; Zawodzinski, T. A.; Harper, D. P., Hierarchical Lignin-Based Carbon Matrix and Carbon Dot Composite Electrodes for High-Performance Supercapacitors. *ACS Omega* **2021**, *6* (11), 7851-7861.
35. Gonzalez-Serrano, E.; Cordero, T.; Rodríguez-Mirasol, J.; Rodríguez, J. J., Development of Porosity upon Chemical Activation of Kraft Lignin with ZnCl₂. *Industrial & Engineering Chemistry Research* **1997**, *36*, 4832-4838.
36. Hayashi, J. i.; Kazehaya, A.; Muroyama, K.; Watkinson, A. P., Preparation of activated carbon from lignin by chemical activation. *Carbon* **2000**, *38*, 1873-1878.
37. Kaneka Techno Research Corporation Page on XPS analysis of chemical state of elements present on a sample surface. https://www.ktr.co.jp/english/zairyuu/z1_sose39.html (accessed July 2022).
38. Western University Canada hosted X-ray Photoelectron Spectroscopy (XPS) Reference Pages. <http://www.xpsfitting.com/2015/11/polyethylene-surfaces.html> (accessed July 2022).
39. Canete, S. J.; Zhang, Z.; Kong, L.; Schlegel, V. L.; Plantz, B. A.; Dowben, P. A.; Lai, R. Y., Application of synchrotron FTIR microspectroscopy for determination of spatial distribution of methylene blue conjugated onto a SAM via "click" chemistry. *Chem Commun (Camb)* **2011**, *47* (43), 11918-20.
40. Meng, X.; Scheidemantle, B.; Li, M.; Wang, Y. Y.; Zhao, X.; Toro-Gonzalez, M.; Singh, P.; Pu, Y.; Wyman, C. E.; Ozcan, S.; Cai, C. M.; Ragauskas, A. J., Synthesis, Characterization, and Utilization of a Lignin-Based Adsorbent for Effective Removal of Azo Dye from Aqueous Solution. *ACS Omega* **2020**, *5* (6), 2865-2877.
41. Yao, Y.; Gao, B.; Inyang, M.; Zimmerman, A. R.; Cao, X.; Pullammanappallil, P.; Yang, L., Removal of phosphate from aqueous solution by biochar derived from anaerobically digested sugar beet tailings. *J Hazard Mater* **2011**, *190* (1-3), 501-7.
42. Li, Y.; Zimmerman, A. R.; He, F.; Chen, J.; Han, L.; Chen, H.; Hu, X.; Gao, B., Solvent-free synthesis of magnetic biochar and activated carbon through ball-mill extrusion with Fe₃O₄ nanoparticles for enhancing adsorption of methylene blue. *Sci Total Environ* **2020**, *722*, 137972.
43. Fierro, V.; Torné-Fernández, V.; Montané, D.; Celzard, A., Adsorption of phenol onto activated carbons having different textural and surface properties. *Microporous and Mesoporous Materials* **2008**, *111* (1-3), 276-284.

44. Wang, G.; Li, G.; Huan, Y.; Hao, C.; Chen, W., Acrylic acid functionalized graphene oxide: High-efficient removal of cationic dyes from wastewater and exploration on adsorption mechanism. *Chemosphere* **2020**, *261*, 127736.
45. Tsai, W. T.; Chang, Y. M.; Lai, C. W.; Lo, C. C., Adsorption of ethyl violet dye in aqueous solution by regenerated spent bleaching earth. *Journal of Colloid and Interface Science* **2005**, *289* (2), 333-338.
46. Yagub, M. T.; Sen, T. K.; Ang, H. M., Equilibrium, Kinetics, and Thermodynamics of Methylene Blue Adsorption by Pine Tree Leaves. *Water, Air, & Soil Pollution* **2012**, *223* (8), 5267-5282.
47. Sprynskyy, M.; Buszewski, B.; Terzyk, A. P.; Namieśnik, J., Study of the selection mechanism of heavy metal (Pb²⁺, Cu²⁺, Ni²⁺, and Cd²⁺) adsorption on clinoptilolite. *Journal of Colloid and Interface Science* **2006**, *304* (1), 21-28.
48. de Guzman, D., Forest2Market page on More R&D Activities Open Up Lignin's Feedstock Potential. <https://www.forest2market.com/blog/more-rd-activities-open-up-lignins-feedstock-potential#:~:text=High%2Dpurity%20lignin%20or%20high,of%20%241300%2D6500%2Fton> (accessed July 2022).
49. Wood Pellet Machine page on Economic Analysis of Coconut Shell Pelletizing. <https://www.biopelletmachine.com/biopellet-making-guidance/build-coconut-shell-pellet-plant.html#:~:text=Commonly%20the%20price%20for%20a,shell%20is%20around%20150%20dollars> (accessed July 2022).
50. Wang, F.; Zhang, J.; Jia, D., Facile synthesis of shell-core structured Fe₃O₄@ACS as recyclable magnetic adsorbent for methylene blue removal. *Journal of Dispersion Science and Technology* **2019**, *40* (12), 1736-1743.
51. Xie, G.; Xi, P.; Liu, H.; Chen, F.; Huang, L.; Shi, Y.; Hou, F.; Zeng, Z.; Shao, C.; Wang, J., A facile chemical method to produce superparamagnetic graphene oxide-Fe₃O₄ hybrid composite and its application in the removal of dyes from aqueous solution. *J. Mater. Chem.* **2012**, *22* (3), 1033-1039.
52. Ai, L.; Jiang, J., Removal of methylene blue from aqueous solution with self-assembled cylindrical graphene-carbon nanotube hybrid. *Chemical Engineering Journal* **2012**, *192*, 156-163.
53. Bestani, B.; Benderdouche, N.; Benstaali, B.; Belhakem, M.; Addou, A., Methylene blue and iodine adsorption onto an activated desert plant. *Bioresource Technology* **2008**, *99* (17), 8441-8444.
54. García-Negrón, V.; Kizzire, D. G.; Rios, O.; Keffer, D. J.; Harper, D. P., Elucidating nano and meso-structures of lignin carbon composites: A comprehensive study of feedstock and temperature dependence. *Carbon* **2020**, *161*, 856-869.
55. Wang, X.; Cheng, H.; Ye, G.; Fan, J.; Yao, F.; Wang, Y.; Jiao, Y.; Zhu, W.; Huang, H.; Ye, D., Key factors and primary modification methods of activated carbon and their application in adsorption of carbon-based gases: A review. *Chemosphere* **2021**, *287* Part 2, 131995.
56. Wan, Z.; Li, K., Effect of pre-pyrolysis mode on simultaneous introduction of nitrogen/oxygen-containing functional groups into the structure of bagasse-based mesoporous carbon and its influence on Cu(II) adsorption. *Chemosphere* **2018**, *194*, 370-380.

TOC:

